


## Positive and Negative Ghost Imaging

Hong-Chao Liu<sup>1,\*</sup>, Huan Yang,<sup>2</sup> Jun Xiong,<sup>2,†</sup> and Shuang Zhang<sup>3,‡</sup>

<sup>1</sup>*Joint Key Laboratory of the Ministry of Education, Institute of Applied Physics and Materials Engineering, University of Macau, Avenida da Universidade, Taipa, Macao SAR, China*

<sup>2</sup>*Department of Physics, Applied Optics Beijing Area Major Laboratory, Beijing Normal University, Beijing 100875, China*

<sup>3</sup>*School of Physics and Astronomy, University of Birmingham, Birmingham B15 2TT, United Kingdom*

 (Received 10 September 2018; revised manuscript received 1 July 2019; published 11 September 2019)

We study the reconstruction-algorithm effect on positive and negative ghost imaging (GI). By introducing three GI algorithms (logarithmic GI, exponential GI, and trigonometric GI), we perform numerical simulations and experiments with different GI algorithms, which demonstrate that a positive or negative ghost image can be recovered by modulating the monotonicity of the object signal function. Our work broadens the GI reconstruction algorithm and deepens the understanding of positive and negative GI principle.

DOI: [10.1103/PhysRevApplied.12.034019](https://doi.org/10.1103/PhysRevApplied.12.034019)

### I. INTRODUCTION

Ghost imaging (GI) is an indirect imaging modality that obtains the object information from the intensity-fluctuation correlation of two beams: one, interacting with the object, is detected by a single-pixel bucket detector, while the other, which carries no object information, is detected by a spatially resolved multipixel detector. Belinsky and Klyshko proposed the concept of GI in 1994 [1] and the early GI experiments were achieved by using the entangled photon pairs generated from a spontaneous parametric down-conversion process [2]. Later, pseudothermal and thermal light sources were successfully applied to reconstruct ghost images [3–9], which initiated a debate on whether GI is a quantum or classical phenomenon. Besides the debate on fundamental physics, GI with different sources and related potential applications has attracted considerable research interest, such as visible and infrared sources for remote sensing and turbulence-free detection [10–15], x-ray and fluorescent sources for medical imaging [16–20], etc. Meanwhile, in order to steer GI toward practical applications, high imaging quality and efficiency have been in great demand, which has sparked lots of studies on GI reconstruction algorithms, including high-order ghost imaging (HGI) [21–30], differential GI [31], compressive ghost imaging (CGI) [32], etc.

Apart from the reconstruction efficiency, different GI algorithms have also significantly affected the type of

the recovered ghost image. For example, a conditional-averaging GI algorithm would generate either a positive or negative ghost image by using different sets of bucket signals [11,33–40]. Nevertheless, the effect of an imaging-reconstruction algorithm on positive and negative GI has not been systematically analyzed so far.

In this work, we study the positive and negative GI principle by investigating the reconstruction-algorithm effect. Here, we introduce three GI algorithms, i.e., logarithmic ghost imaging (LGI), exponential ghost imaging (EGI), and trigonometric ghost imaging (TGI). We theoretically and experimentally compare them with previous algorithms in the positive and negative GI processes. Simulation and experiment results show that a positive or negative ghost image can be reconstructed by modulating the monotonicity of the object signal function in each algorithm.

### II. THEORY AND SIMULATION ON POSITIVE AND NEGATIVE GHOST IMAGING

In general, the second-order correlation function of two signals is defined as follows [41]:

$$G^{(2)}(r_1, r_2) = \langle I(r_1)I(r_2) \rangle, \quad (1)$$

where  $I(r_1)$  and  $I(r_2)$  are the instantaneous intensities at positions  $r_1$  and  $r_2$ , respectively.  $\langle \dots \rangle$  denotes the ensemble average. For simplicity, only the spatial correlation is taken into consideration here but the following results and discussions are also valid for the temporal one. Basically, the image reconstruction of GI originates from the spatial distribution of  $G^{(2)}(r_1, r_2)$  values, manifesting a unified

\*hcliu@um.edu.mo

†junxiong@bnu.edu.cn

‡s.zhang@bham.ac.uk

approach between GI and a fundamental experiment performed by Hanbury Brown and Twiss (HBT) [42,43]. Similar to the critical role of the wave source in the HBT experiment, different types of source will result in either a positive or a negative ghost image. For chaotic bosons and fermions, the second-order correlation function in Eq. (1) can be further expanded as follows [44–46]:

$$G^{(2)}(r_1, r_2) = G^{(1)}(r_1, r_1)G^{(1)}(r_2, r_2) \pm |G^{(1)}(r_1, r_2)|^2, \quad (2)$$

where  $G^{(1)}(r_i, r_j)$  ( $i, j = 1, 2$ ) represents the first-order correlation function and the + and – signs are for the bosonic and fermionic sources, respectively. In the HBT experiment,  $+|G^{(1)}(r_1, r_2)|^2$  leads to a bunching effect, whereas  $-|G^{(1)}(r_1, r_2)|^2$  results in an antibunching behavior. Correspondingly, in GI, a bosonic source provides a positive (bright) ghost image, whereas a fermionic source offers a negative (dark) one [45,46].

As well as sources of different types, sources with different statistical distributions will also affect the type of GI [47]. For the pseudothermal (or thermal) light and the entangled photon pairs from spontaneous parametric down-conversion, the sources are governed by super-Poissonian statistics with a statistical distribution  $\Delta n_p^2 > \langle n_p \rangle$ , where  $n_p$  is the particle number and  $\Delta n_p^2 = \langle n_p^2 \rangle - \langle n_p \rangle^2$  is the mean-square deviation of  $n_p$ . These super-Poissonian sources will generate positive ghost images. In the opposite case, when the source obeys sub-Poissonian statistics, i.e.,  $\Delta n_p^2 < \langle n_p \rangle$ , an antibunching behavior will appear, resulting in a negative ghost image. As a Poissonian source obeys  $\Delta n_p^2 = \langle n_p \rangle$ , no ghost image can be obtained.

In addition to the above source effect, different GI algorithms can also determine whether a positive or negative ghost image will be recovered. Assuming that the source is a bosonic one that obeys super-Poissonian statistics, we will focus on the impact of GI algorithms on the positive and negative GI in the following.

According to Eq. (1), the traditional second-order GI reconstruction algorithm can be expressed as follows:

$$G^{(2)}(x, y) = \frac{1}{N} \sum_{i=1}^N I_{o_i} I_i(x, y), \quad (3)$$

where  $I_{o_i}$  is the bucket-intensity signal of the object beam and  $I_i(x, y)$  is the intensity distribution at position  $(x, y)$  of the reference beam in the  $i$ th measurement. The schematic setup of GI is shown in Fig. 1. Based on Eq. (3), conditional-averaging GI has been introduced to achieve positive and negative ghost images[11,33–40]. In conditional-averaging GI, the object signals are divided into two sets: for  $I_{o_i}$  satisfying  $I_{o_i} \geq \bar{I}_o$ , Eq. (3) provides a

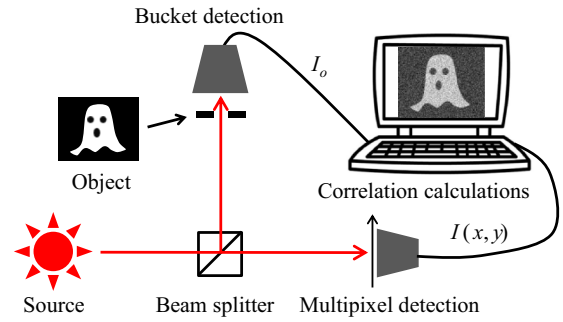


FIG. 1. The schematic setup of two-detector ghost imaging.

positive ghost image; and for  $I_{o_i}$  satisfying  $I_{o_i} < \bar{I}_o$ , a negative ghost image appears, where  $\bar{I}_o$  is the average intensity of the object signals over  $N$  measurements.

Usually, an average-intensity subtraction (AIS) of a object signal can provide a better GI quality. The reconstruction algorithm is given as follows:

$$G^{(2)}(x, y) = \frac{1}{N} \sum_{i=1}^N I_{o_i}^{\text{AIS}} I_i(x, y), \quad (4)$$

where  $I_{o_i}^{\text{AIS}} = I_{o_i} - \bar{I}_o$ . Differently, after subtracting  $\bar{I}_o$  in Eq. (4), the above positive and negative GI operation in conditional-averaging GI becomes invalid, since both sets of bucket signals (i.e.,  $I_{o_i}^{\text{AIS}} < 0$  and  $I_{o_i}^{\text{AIS}} \geq 0$ ) always provide positive ghost images. Thus, to obtain a negative image based on Eq. (4),  $I_{o_i}^{\text{AIS}}$  should take an opposite sign, that is,  $-I_{o_i}^{\text{AIS}}$ .

In comparison to the above conditional-averaging GI and GI with AIS, the HGI algorithm reconstructs the positive and negative ghost images based on its power-index value. The most-used form of the HGI algorithm is defined as follows [24,26,28,30]:

$$G^{(p,q)}(x, y) = \frac{1}{N} \sum_{i=1}^N (I_{o_i})^p [I_i(x, y)]^q, \quad (5)$$

where  $p$  and  $q$  are the power indices of the object signal and the reference signal, respectively. Usually,  $p$  and  $q$  are positive integers, in which case a positive ghost image is achieved. A recent study has shown that  $p$  and  $q$  could even take negative and fractional values [48]. When  $pq < 0$ , a negative ghost image will be recovered.

Besides the two above approaches, LGI and EGI algorithms are introduced here to study positive and negative GI. We define the LGI algorithm as follows:

$$G^{\log}(x, y) = \frac{1}{N} \sum_{i=1}^N \left( \log_A \frac{I_{o_i}}{\bar{I}_o} \right) I_i(x, y), \quad (6)$$

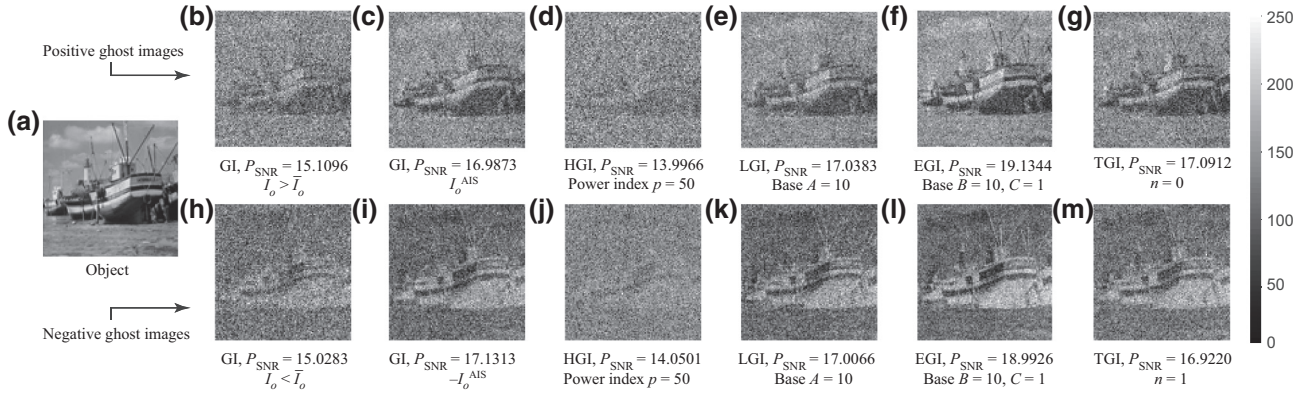


FIG. 2. Simulation results of positive and negative ghost images with different algorithms: (a) object; (b),(h) traditional ghost imaging; (c),(i) ghost imaging with AIS; (d),(j) high-order ghost imaging; (e),(k) logarithmic ghost imaging; (f),(l) exponential ghost imaging; (g),(m) trigonometric ghost imaging.

where  $A$  is the base of the logarithmic function. The other algorithm, EGI, is defined as follows:

$$G^{\text{exp}}(x, y) = \frac{1}{N} \sum_{i=1}^N B^{C(I_{o_i}/S_i)} I_i(x, y), \quad (7)$$

where  $B$  is the base of the exponential function,  $C$  is a constant depending on the value of base  $B$ , and  $S_i$  is the total intensity of reference beam  $I_i(x, y)$  in the  $i$ th measurement, i.e.,  $S_i = \int I_i(x, y) dx dy$ . Different from previous algorithms, LGI and EGI use their base values to control the type of GI. When the base value is greater (smaller) than 1, a positive (negative) ghost image will be obtained.

Moreover, another algorithm, TGI, can also achieve both positive and negative GI. For example, we define the TGI in a sinusoidal form as follows:

$$G^{\text{sin}}(x, y) = \frac{1}{N} \sum_{i=1}^N \sin \left[ \left( n + I'_{o_i} - \frac{1}{2} \right) \pi \right] I_i(x, y), \quad (8)$$

where  $I'_{o_i} = (I_{o_i} - I_{\min}) / (I_{\max} - I_{\min})$  and  $I_{\max}$  and  $I_{\min}$  are the maximum and minimum of  $I_{o_i}$ , respectively. In TGI,  $n$  takes even (odd) integers, leading to a positive (negative) ghost image.

Figure 2 shows the simulation results of positive and negative GI with different algorithms. A grayscale boat picture ( $101 \times 101$  pixels) acts as the imaging object, as shown in Fig. 2(a). In the simulation, we set  $p = 50$  and  $q = 1$  for the HGI algorithm, because a large  $p$  value would increase the image visibility and a small  $q$  would suppress the noise dramatically [26,28,30]. In both the LGI and the EGI algorithms, we set base  $A, B = 10$  ( $A, B = 0.1$ ) for the positive (negative) GI processes and a constant  $C = 1$  is adopted in the EGI case. In the TGI algorithms,  $n = 0$  is set for positive GI and  $n = 1$  for negative GI. The measurement number is set as 80 000 for all algorithms.

Here, we employ a peak signal-to-noise ratio ( $P_{\text{SNR}}$ ) to estimate the image quality, which is defined as follows:

$$P_{\text{SNR}} = 10 \log_{10} \left( \frac{M_{\max}}{M_{\text{mse}}} \right), \quad (9)$$

where  $M_{\max} = 255$  is the maximum possible pixel value of the image.  $M_{\text{mse}}$  is the mean square error, given by  $(1/(m_1 \times m_2)) \sum_{i,j} [T_{\text{re}}(x_i, y_j) - T(x_i, y_j)]^2$ , where  $m_1 \times m_2$  is the pixel number and  $T_{\text{re}}(x_i, y_j)$  and  $T(x_i, y_j)$  are the pixel values of the recovered image and the object, respectively.

Figures 2(b) and 2(h) show the positive and negative images recovered from the conditional-averaging GI, respectively. Since only half signals ( $I_{o_i} > \bar{I}_o$  or  $I_{o_i} < \bar{I}_o$ ) are available for the reconstruction calculations, the imaging quality is worse than the cases of GI with AIS, LGI, EGI, and TGI. Although the HGI algorithm can also obtain the positive and negative images shown in Figs. 2(d) and 2(j), it has a low imaging efficiency. This is because a high-order correlation on the bucket-intensity signal will enhance the information signal but at the same time increase the background noise. This low efficiency can, however, be improved by replacing the object signal  $(I_{o_i})^p$  with an AIS one, i.e.,  $(I_{o_i})^p - (\bar{I}_o)^p$ . The comparison between different algorithms in Fig. 2 manifests that EGI offers better quality, and GI with AIS, LGI, and TGI have similar reconstruction efficiencies in both the positive and negative GI processes.

To clearly reveal the positive and negative GI principle, the object signals (50 measurements) of the different algorithms are presented in Fig. 3. According to the definition of GI, the reference signal  $I_i(x, y)$  and the object signal  $I_{o_i}$  are in one-to-one correspondence. In order to improve the imaging-reconstruction efficiency, different functions  $f(I_{o_i})$  are usually introduced to replace the object signal. No matter what specific form  $f(I_{o_i})$  takes, the type of ghost

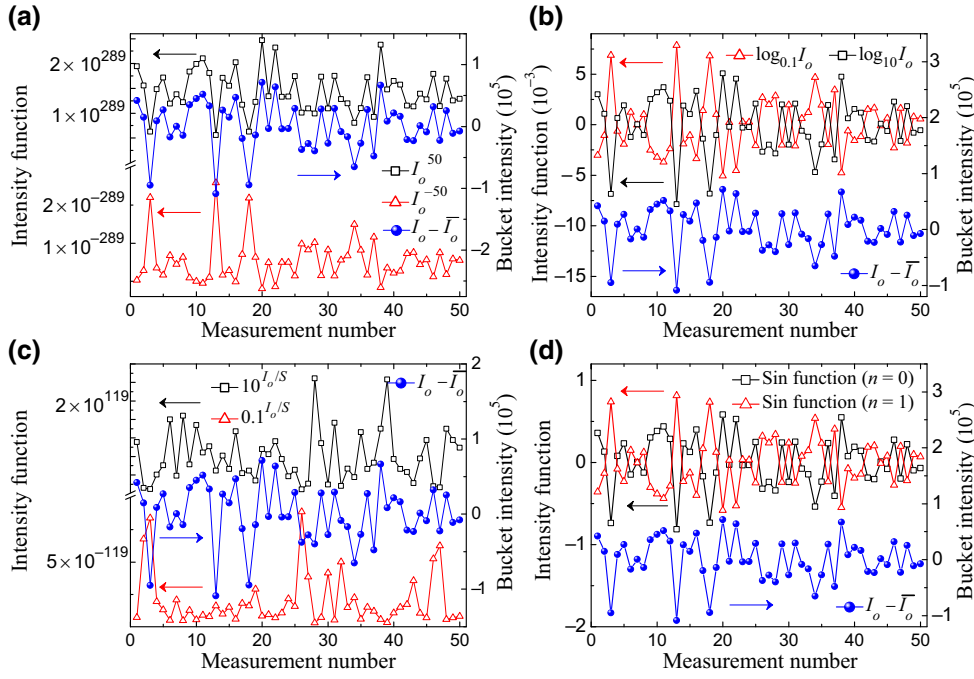


FIG. 3. Simulation results of intensity signals with different GI algorithms: (a) HGI, (b) LGI, (c) EGI, and (d) TGI. When the power index  $p = 50$  in HGI, the base value  $A = 10$  in LGI, the base value  $B = 10$  in EGI, and  $n = 0$  in TGI, the intensity functions follow the same variation trend as the bucket intensity. On the contrary, when  $p = -50$ ,  $A = 0.1$ ,  $B = 0.1$ , and  $n = 1$ , an opposite variation trend of the intensity functions is seen.

image is determined by the monotonicity of  $f(I_{o_i})$ . If  $f(I_{o_i})$  is monotonically increasing (decreasing) as  $I_{o_i}$  increases, a positive (negative) image will be obtained. From Figs. 3(a), 3(b), and 3(d), when the power index  $p > 0$  in HGI, the base value  $A > 1$  in LGI, and  $n = 0$  in TGI, this clearly shows that the  $f(I_{o_i})$  intensity functions have the same variation trend as the original object signal  $I_{o_i}$ , leading to positive images. On the contrary, when  $p < 0$ ,  $A < 1$ , and  $n = 1$ , a completely opposite trend of  $f(I_{o_i})$  is exhibited, resulting in negative images. In particular, in the EGI algorithm,  $I_{o_i}/S_i$  acts as the power index. Since  $S_i$  always changes with the measuring times  $i$ ,  $f(I_{o_i}) = B^{I_{o_i}/S_i}$  does not follow a strict monotonicity to  $I_{o_i}$ , as shown in Fig. 3(c). Nevertheless, the overall trend of  $f(I_{o_i})$  in EGI is determined by the base value, as discussed in the LGI case above. This nonstrict monotonicity of EGI is similar to the differential GI algorithm with  $f(I_{o_i}) = I_{o_i} - \bar{I}_o S_i / \bar{S}_i$  [31], which may explain the better imaging quality of EGI shown in Fig. 2. Table I summarizes the parameters used in the various algorithms to achieve positive and negative ghost images.

Compared to the monotonicity-dependent principle, conditional-averaging GI works well in the basic GI definition  $\langle I_o I(x, y) \rangle$ , but is ineffective in GI with the AIS, LGI, EGI, and TGI algorithms, due to its background-dependent nature. Moreover, it should be mentioned that here we only discuss the monotonicity of the object signal function  $f(I_{o_i})$ . Alternatively, one can keep the object signal  $I_{o_i}$  unchanged and modulate the monotonicity of the reference signal  $I_i(x, y)$  to control whether a positive or negative ghost image is recovered. In addition, since all the above discussions are based on a photonic source with

super-Poissonian statistics, the above principle of monotonicity dependence will lead to an opposite result for a bosonic source with sub-Poissonian statistics or a chaotic fermionic source.

To further understand the effect of the monotonicity-dependent principle on positive and negative GI, we can go back to the definition of GI. In Eq. (3), the reconstructed image  $G^{(2)}(x, y)$  can be viewed as a Fourier expansion, where the reference signal  $I_i(x, y)$  represents the base, the bucket signal  $I_{o_i}$  represents the corresponding coefficient as  $I_{o_i} = \sum_{x=1}^{m_1} \sum_{y=1}^{m_2} O(x, y) I_i(x, y)$ , and  $O(x, y)$  is the original object image function. As a simplest case, we here suppose that the original image only consists of two pixels, i.e.,  $[O(1, 1), O(1, 2)]$ , and the reference signals are mutually orthogonal, i.e.,  $I_1(x, y) = [1, 0]$  and  $I_2(x, y) = [0, 1]$ . Therefore, according to Eq. (3), one can easily obtain that  $G^{(2)}(x, y) = [O(1, 1), O(1, 2)]/2$  after two measurements. Suppose that  $O(1, 1) > O(1, 2)$  in the original image;  $G^{(2)}(x, y)$  thereby recovers a positive image. Now, if  $I_{o_i}$  is replaced by  $f(I_{o_i})$ , the reconstructed image will be  $G^{(2)}(x, y) = \{f[O(1, 1)], f[O(1, 2)]\}/2$ . Due to the

TABLE I. Parameters to generate positive and negative ghost images in different algorithms.

GI algorithms	Positive GI	Negative GI
GI: $\langle I_o I(x, y) \rangle$	$I_o (I_o \geq \bar{I}_o)$	$I_o (I_o < \bar{I}_o)$
GI with AIS: $\langle (I_o - \bar{I}_o) I(x, y) \rangle$	$I_o - \bar{I}_o$	$\bar{I}_o - I_o$
HGI: $\langle (I_o)^p [I(x, y)]^q \rangle$	$pq > 0$	$pq < 0$
LGI: $\langle (\log_A I_o / \bar{I}_o) I(x, y) \rangle$	$A > 1$	$A < 1$
EGI: $\langle B^{C(I_o/S)} I(x, y) \rangle$	$B^C > 1$	$B^C < 1$
TGI: $\langle \sin[(n + I_o - 1/2)\pi] I(x, y) \rangle$	$n$ is even	$n$ is odd



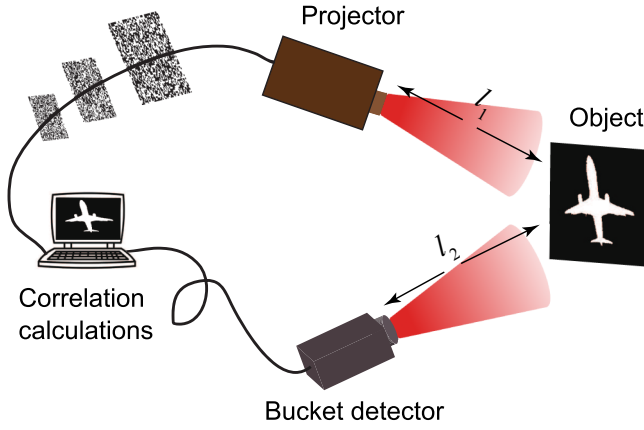


FIG. 4. The experimental setup of computational ghost imaging.

monotonicity-dependent principle,  $G^{(2)}(x, y)$  will result in a positive (negative) ghost image when  $f(I_{oi})$  is a monotonic increasing (decreasing) function. Note that, in mathematics, the bases in a Fourier expansion should always be mutually orthogonal. But in GI, the bases are random light speckles, which are usually nonorthogonal. These nonorthogonal bases will make  $I_{oi}$  complicated—which, however, will not affect the validity of the monotonicity-dependent principle when the measurement number  $N$  is large enough. A more complicated  $2 \times 2$  pixels case with nonorthogonal bases is discussed in the Appendix.

### III. EXPERIMENT ON POSITIVE AND NEGATIVE GHOST IMAGING

All of the above GI algorithms can work within the traditional two-detector GI experimental framework.

Compared to the two-detector GI setup shown in Fig. 1, computational GI introduces a known random matrix  $X_i^{m_1 \times m_2}$  to replace the reference beam  $I_i(x, y)$  [49]. Since the random matrix  $X_i^{m_1 \times m_2}$  can be generated by liquid-crystal spatial light modulators, digital micromirror devices, or projectors [14, 49–52], just a single-pixel detector is sufficient for the computational GI experiment. By employing the computational GI scheme, we experimentally test the reconstruction-algorithm effect on positive and negative GI below. Our experimental setup is shown in Fig. 4. A standard projector with  $1024 \times 768$  pixels is used to generate the random matrices. For simplicity, an independent speckle consists of  $16 \times 16$  pixels among total  $1024 \times 768$  pixels, so there are only  $64 \times 48$  speckles in one frame [38]. After being reflected by the object (a model of an airplane), the reflected beam is bucket collected by a single-pixel detector, where  $l_1 = 70$  cm and  $l_2 = 100$  cm. The exposure time of the detector is 400 ms and the sampling number in the experiment is 23 000.

Figure 5 shows the experimental ghost images recovered from the various GI algorithms. Consistent with the simulation results in Fig. 2, one can see that the imaging quality of HGI and conditional-averaging GI is worse than that of the other algorithms. It should be noted that, for the same set of measurement data, the  $P_{\text{SNR}}$  values of the positive and negative ghost images in GI with AIS are the same. This is because the only difference between their object signal functions  $f(I_{oi})$  is an opposite sign, i.e.,  $f_P(I_{oi}) = (I_{oi} - \bar{I}_o) = -f_N(I_{oi})$ . This is also the case for LGI, i.e.,  $f_P(I_{oi}) = \log_{10}(I_{oi}/\bar{I}_o) = -\log_{0.1}(I_{oi}/\bar{I}_o) = -f_N(I_{oi})$ , and for TGI, i.e.,  $f_P(I_{oi}) = \sin[(0 + I'_o - 1/2)\pi] = -\sin[(1 + I'_o - 1/2)\pi] = -f_N(I_{oi})$ . After normalizing the positive and negative GI

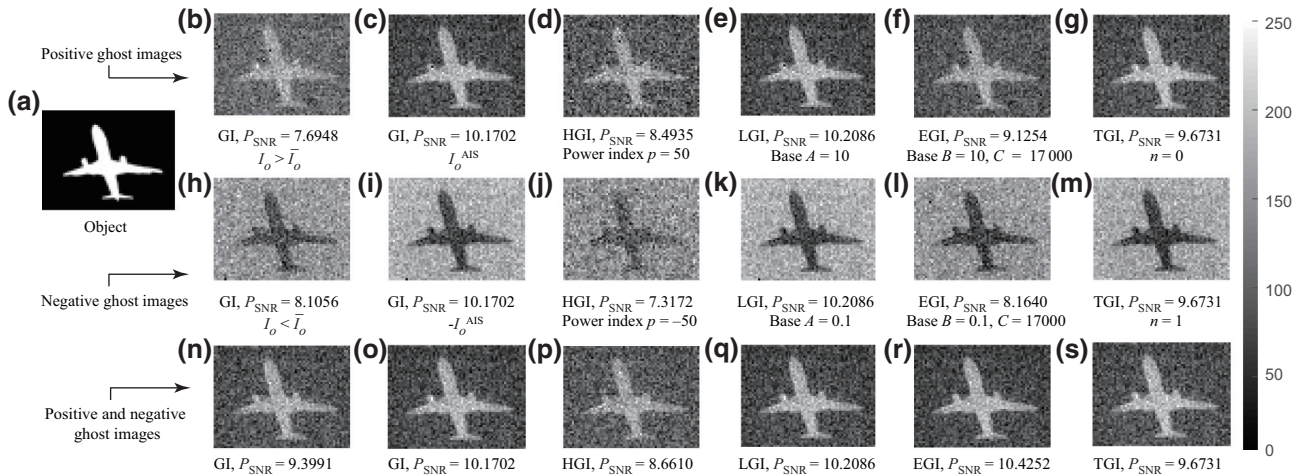


FIG. 5. Experimental positive-negative ghost images with different algorithms: (a) object; (b),(h) traditional ghost imaging; (c),(i) ghost imaging with AIS; (d),(j) high-order ghost imaging; (e),(k) logarithmic ghost imaging; (f),(l) exponential ghost imaging; (g),(m) trigonometric ghost imaging. (n)–(s) Ghost images obtained from subtracting the negative one from the corresponding positive one.

images, respectively, we perform a further operation, i.e., subtracting the negative image from the corresponding positive one. As shown in Figs. 5(n)–5(s), the qualities of the subtracted ghost images in conditional-averaging GI, HGI, and EGI have been improved. This phenomenon has been reported and discussed in conditional-averaging GI [34,36,40]. Different from conditional-averaging GI, this normalized subtraction operation in HGI and EGI effectively suppress the noise in their divergence reconstruction calculations, which therefore increases the image quality. Since the positive and negative ghost images have the same  $P_{\text{SNR}}$  values in GI with AIS, LGI, and TGI, as mentioned above, no improvements are made in these three algorithms by applying the subtraction operation.

#### IV. CONCLUSION

In conclusion, we study positive and negative GI by analyzing the imaging-reconstruction-algorithm effect. Three GI algorithms (LGI, EGI, and TGI) are proposed and studied both in simulation and experiment. By comparing them with various other GI algorithms, we demonstrate that a positive or negative ghost image can be recovered by modulating the monotonicity of the object signal function. Our proposed GI algorithms and positive and negative GI principle gain the knowledge of GI.

#### ACKNOWLEDGMENTS

This work is financially supported by a European Research Council Consolidator Grant (TOPOLOGICAL), Project No. 648783. S.Z. acknowledges support from the Royal Society and the Wolfson Foundation. J.X. is supported by the National Natural Science Foundation of China under Grants No. 11474027 and No. 11735005 and by the Interdiscipline Research Funds of Beijing Normal University.

Hong-Chao Liu and Huan Yang contributed equally to this work.

#### APPENDIX

As an example, an image with a  $2 \times 2$  pixels case is discussed below. The original object image function is as follows:

$$O(x,y) = \begin{bmatrix} O(1,1) & O(1,2) \\ O(2,1) & O(2,2) \end{bmatrix}. \quad (\text{A1})$$

Suppose that the reference signals are random binary matrices. There are 16 possible nonorthogonal bases with

the same probability of occurrence during the measurement:

$$I(x,y) = \begin{bmatrix} 1 & 0 \\ 0 & 0 \end{bmatrix}, \begin{bmatrix} 0 & 1 \\ 0 & 0 \end{bmatrix}, \begin{bmatrix} 0 & 0 \\ 1 & 0 \end{bmatrix}, \begin{bmatrix} 0 & 0 \\ 0 & 1 \end{bmatrix}, \\ \begin{bmatrix} 1 & 1 \\ 0 & 0 \end{bmatrix}, \begin{bmatrix} 0 & 1 \\ 1 & 0 \end{bmatrix}, \begin{bmatrix} 0 & 0 \\ 1 & 1 \end{bmatrix}, \begin{bmatrix} 1 & 0 \\ 0 & 1 \end{bmatrix}, \\ \begin{bmatrix} 1 & 0 \\ 1 & 0 \end{bmatrix}, \begin{bmatrix} 0 & 1 \\ 0 & 1 \end{bmatrix}, \begin{bmatrix} 0 & 1 \\ 1 & 1 \end{bmatrix}, \begin{bmatrix} 1 & 0 \\ 1 & 1 \end{bmatrix}, \\ \begin{bmatrix} 1 & 1 \\ 0 & 1 \end{bmatrix}, \begin{bmatrix} 1 & 1 \\ 1 & 0 \end{bmatrix}, \begin{bmatrix} 1 & 1 \\ 1 & 1 \end{bmatrix}, \begin{bmatrix} 0 & 0 \\ 0 & 0 \end{bmatrix}. \quad (\text{A2})$$

After 16 measurements with the above different reference signals, one can obtain the reconstructed ghost image as follows:

$$G^{(2)}(x,y) = \frac{1}{16} \begin{bmatrix} G^{(2)}(1,1) & G^{(2)}(1,2) \\ G^{(2)}(2,1) & G^{(2)}(2,2) \end{bmatrix}, \quad (\text{A3})$$

where

$$G^{(2)}(1,1) = f [O(1,1)] + f [O(1,1) + O(1,2)] \\ + f [O(1,1) + O(2,1)] + f [O(1,1) + O(2,2)] \\ + f [O(1,1) + O(1,2) + O(2,1)] \\ + f [O(1,1) + O(1,2) + O(2,2)] \\ + f [O(1,1) + O(2,1) + O(2,2)] \\ + f [O(1,1) + O(1,2) + O(2,1) + O(2,2)], \quad (\text{A4})$$

$$G^{(2)}(1,2) = f [O(1,2)] + f [O(1,2) + O(1,1)] \\ + f [O(1,2) + O(2,1)] + f [O(1,2) + O(2,2)] \\ + f [O(1,2) + O(1,1) + O(2,1)] \\ + f [O(1,2) + O(1,1) + O(2,2)] \\ + f [O(1,2) + O(2,1) + O(2,2)] \\ + f [O(1,1) + O(1,2) + O(2,1) + O(2,2)], \quad (\text{A5})$$

$$G^{(2)}(2,1) = f [O(2,1)] + f [O(2,1) + O(1,1)] \\ + f [O(2,1) + O(1,2)] + f [O(2,1) + O(2,2)] \\ + f [O(2,1) + O(1,1) + O(1,2)] \\ + f [O(2,1) + O(1,1) + O(2,2)] \\ + f [O(2,1) + O(1,2) + O(2,2)] \\ + f [O(1,1) + O(1,2) + O(2,1) + O(2,2)], \quad (\text{A6})$$

$$\begin{aligned}
 G^{(2)}(2, 2) = & f [O(2, 2)] + f [O(2, 2) + O(1, 1)] \\
 & + f [O(2, 2) + O(1, 2)] + f [O(2, 2) + O(2, 1)] \\
 & + f [O(2, 2) + O(1, 1) + O(1, 2)] \\
 & + f [O(2, 2) + O(1, 1) + O(2, 1)] \\
 & + f [O(2, 2) + O(1, 2) + O(2, 1)] \\
 & + f [O(1, 1) + O(1, 2) + O(2, 1) + O(2, 2)].
 \end{aligned}
 \tag{A7}$$

By assuming that  $O(1, 1) > O(1, 2) > O(2, 1) > O(2, 2)$  in the original object image function, one can clearly see that  $G^{(2)}(1, 1) > G^{(2)}(1, 2) > G^{(2)}(2, 1) > G^{(2)}(2, 2)$  [or  $G^{(2)}(1, 1) < G^{(2)}(1, 2) < G^{(2)}(2, 1) < G^{(2)}(2, 2)$ ] for a monotonic increasing (or decreasing) function  $f [O(x, y)]$ , after comparing Eqs. (A4)–(A7). This means that a positive (or negative) ghost image can be obtained by following our monotonicity-dependent principle.

- 
- [1] A. V. Belinsky and D. N. Klyshko, Two-photon optics: Diffraction, holography, and transformation of two-dimensional signals, *Sov. Phys. JETP* **78**, 259 (1994).
- [2] T. B. Pittman, Y. H. Shih, D. V. Strekalov, and A. V. Sergienko, Optical imaging by means of two-photon quantum entanglement, *Phys. Rev. A* **52**, R3429 (1995).
- [3] R. S. Bennink, S. J. Bentley, and R. W. Boyd, “Two-Photon” Coincidence Imaging with a Classical Source, *Phys. Rev. Lett.* **89**, 113601 (2002).
- [4] K. Wang and D.-Z. Cao, Subwavelength coincidence interference with classical thermal light, *Phys. Rev. A* **70**, 041801(R) (2004).
- [5] F. Ferri, D. Magatti, A. Gatti, M. Bache, E. Brambilla, and L. A. Lugiato, High-Resolution Ghost Image and Ghost Diffraction Experiments with Thermal Light, *Phys. Rev. Lett.* **94**, 183602 (2005).
- [6] A. Valencia, G. Scarcelli, M. D’Angelo, and Y. Shih, Two-Photon Imaging with Thermal Light, *Phys. Rev. Lett.* **94**, 063601 (2005).
- [7] J. Xiong, D.-Z. Cao, F. Huang, H.-G. Li, X.-J. Sun, and K. Wang, Experimental Observation of Classical Subwavelength Interference with a Pseudothermal Light Source, *Phys. Rev. Lett.* **94**, 173601 (2005).
- [8] Y. Cai and S.-Y. Zhu, Ghost imaging with incoherent and partially coherent light radiation, *Phys. Rev. E* **71**, 056607 (2005).
- [9] X.-H. Chen, Q. Liu, K.-H. Luo, and L.-A. Wu, Lensless ghost imaging with true thermal light, *Opt. Lett.* **34**, 695 (2009).
- [10] J. Cheng, Ghost imaging through turbulent atmosphere, *Opt. Exp.* **17**, 7916 (2009).
- [11] R. E. Meyers, K. S. Deacon, and Y. Shih, Positive-negative turbulence-free ghost imaging, *Appl. Phys. Lett.* **100**, 131114 (2012).
- [12] C. Zhao, W. Gong, M. Chen, E. Li, H. Wang, W. Xu, and S. Han, Ghost imaging lidar via sparsity constraints, *Appl. Phys. Lett.* **101**, 141123 (2012).
- [13] M. P. Edgar, G. M. Gibson, R. W. Bowman, B. Sun, N. Radwell, K. J. Mitchell, S. S. Welsh, and M. J. Padgett, Simultaneous real-time visible and infrared video with single-pixel detectors, *Sci. Rep.* **5**, 10669 (2015).
- [14] M.-J. Sun, M. P. Edgar, G. M. Gibson, B. Q. Sun, N. Radwell, R. Lamb, and M. J. Padgett, Single-pixel three-dimensional imaging with time-based depth resolution, *Nat. Commun.* **7**, 12010 (2016).
- [15] H.-C. Liu and S. Zhang, Computational ghost imaging of hot objects in long-wave infrared range, *Appl. Phys. Lett.* **111**, 031110 (2017).
- [16] H. Yu, R. Lu, S. Han, H. Xie, G. Du, T. Xiao, and D. Zhu, Fourier-Transform Ghost Imaging with Hard X Rays, *Phys. Rev. Lett.* **117**, 113901 (2016).
- [17] D. Pelliccia, A. Rack, M. Scheel, V. Cantelli, and D. M. Paganin, Experimental X-Ray Ghost Imaging, *Phys. Rev. Lett.* **117**, 113902 (2016).
- [18] A.-X. Zhang, Y.-H. He, L.-A. Wu, L.-M. Chen, and B.-B. Wang, Tabletop x-ray ghost imaging with ultra-low radiation, *Optica* **5**, 374 (2018).
- [19] N. Tian, Q. Guo, A. Wang, D. Xu, and L. Fu, Fluorescence ghost imaging with pseudothermal light, *Opt. Lett.* **36**, 3302 (2011).
- [20] R. I. Khakimov, B. M. Henson, D. K. Shin, S. S. Hodgman, R. G. Dall, K. G. H. Baldwin, and A. G. Truscott, Ghost imaging with atoms, *Nature* **540**, 100 (2016).
- [21] W. Chen and X. D. Chen, Marked ghost imaging, *Appl. Phys. Lett.* **104**, 251109 (2014).
- [22] Y. Bai and S. Han, Ghost imaging with thermal light by third-order correlation, *Phys. Rev. A* **76**, 043828 (2007).
- [23] I. N. Agafonov, M. V. Chekhova, T. S. Iskhakov, and A. N. Penin, High-visibility multiphoton interference of Hanbury Brown-Twiss type for classical light, *Phys. Rev. A* **77**, 053801 (2008).
- [24] D.-Z. Cao, J. Xiong, S.-H. Zhang, L.-F. Lin, L. Gao, and K. Wang, Enhancing visibility and resolution in  $N$ th-order intensity correlation of thermal light, *Appl. Phys. Lett.* **92**, 201102 (2008).
- [25] J. Liu and Y. Shih,  $N$ th-order coherence of thermal light, *Phys. Rev. A* **79**, 023819 (2009).
- [26] K. W. C. Chan, M. N. O’Sullivan, and R. W. Boyd, High-order thermal ghost imaging, *Opt. Lett.* **34**, 3343 (2009).
- [27] Q. Liu, X.-H. Chen, K.-H. Luo, W. Wu, and L.-A. Wu, Role of multiphoton bunching in high-order ghost imaging with thermal light sources, *Phys. Rev. A* **79**, 053844 (2009).
- [28] X.-H. Chen, I. N. Agafonov, K.-H. Luo, Q. Liu, R. Xian, M. V. Chekhova, and L.-A. Wu, High-visibility, high-order lensless ghost imaging with thermal light, *Opt. Lett.* **35**, 1166 (2010).
- [29] Y.-C. Liu and L.-M. Kuang, Theoretical scheme of thermal-light many-ghost imaging by  $N$ th-order intensity correlation, *Phys. Rev. A* **83**, 053808 (2011).
- [30] H.-C. Liu and J. Xiong, Properties of high-order ghost imaging with natural light, *J. Opt. Soc. Am. A* **30**, 956 (2013).
- [31] F. Ferri, D. Magatti, L. A. Lugiato, and A. Gatti, Differential Ghost Imaging, *Phys. Rev. Lett.* **104**, 253603 (2010).
- [32] O. Katz, Y. Bromberg, and Y. Silberberg, Compressive ghost imaging, *Appl. Phys. Lett.* **95**, 131110 (2009).
- [33] L.-A. Wu and K.-H. Luo, Two-photon imaging with entangled and thermal light, *AIP Conf. Proc.* 1384, 223 (2011).

- [34] K.-H. Luo, B.-Q. Huang, W.-M. Zheng, and L.-A. Wu, Nonlocal imaging by conditional averaging of random reference measurements, *Chin. Phys. Lett.* **29**, 074216 (2012).
- [35] J. Wen, Forming positive-negative images using conditioned partial measurements from reference arm in ghost imaging, *J. Opt. Soc. Am. A* **29**, 1906 (2012).
- [36] W.-K. Yu, X.-R. Yao, X.-F. Liu, L.-Z. Li, and G.-J. Zhai, Ghost imaging based on Pearson correlation coefficients, *Chin. Phys. B* **24**, 054203 (2015).
- [37] X.-R. Yao, X.-F. Liu, W.-K. Yu, and G.-J. Zhai, Correspondence imaging based on correlation coefficients, *Chin. Opt. Lett.* **13**, 010301 (2015).
- [38] H. Yang, S. Wu, H.-B. Wang, D.-Z. Cao, S.-H. Zhang, J. Xiong, and K. Wang, Probability theory in conditional-averaging ghost imaging with thermal light, *Phys. Rev. A* **98**, 053853 (2018).
- [39] C. Gao, X. Q. Wang, Z. F. Wang, Z. Li, G. J. Du, F. Chang, and Z. H. Yao, Optimization of computational ghost imaging, *Phys. Rev. A* **96**, 023838 (2017).
- [40] S.-C. Song, M.-J. Sun, and L.-A. Wu, Improving the signal-to-noise ratio of thermal ghost imaging based on positive-negative intensity correlation, *Opt. Commun.* **366**, 8 (2016).
- [41] J. W. Goodman, *Statistical Optics* (Wiley, New York, 1985).
- [42] R. Hanbury Brown and R. Q. Twiss, The question of correlation between photons in coherent light rays, *Nature* **178**, 1046 (1956).
- [43] L.-G. Wang, S. Qamar, S.-Y. Zhu, and M. S. Zubairy, Hanbury Brown-Twiss effect and thermal light ghost imaging: A unified approach, *Phys. Rev. A* **79**, 033835 (2009).
- [44] K. E. Cahill and R. J. Glauber, Density operators for fermions, *Phys. Rev. A* **59**, 1538 (1999).
- [45] S. Gan, D.-Z. Cao, and K. Wang, Dark quantum imaging with fermions, *Phys. Rev. A* **80**, 043809 (2009).
- [46] H.-C. Liu, High-order correlation of chaotic bosons and fermions, *Phys. Rev. A* **94**, 023827 (2016).
- [47] K. W. C. Chan, Role of photon statistics of light source in ghost imaging, *Opt. Lett.* **37**, 2739 (2012).
- [48] D.-Z. Cao, Q.-C. Li, X.-C. Zhuang, C. Ren, S.-H. Zhang, and X.-B Song, Ghost images reconstructed from fractional-order moments with thermal light, *Chin. Phys. B* **27**, 123401 (2018).
- [49] J. H. Shapiro, Computational ghost imaging, *Phys. Rev. A* **78**, 061802(R) (2008).
- [50] P. Clemente, V. Durán, E. Tajahuerce, and J. Lancis, Optical encryption based on computational ghost imaging, *Opt. Lett.* **35**, 2391 (2010).
- [51] D. Duan, S. Du, and Y. Xia, Multiwavelength ghost imaging, *Phys. Rev. A* **88**, 053842 (2013).
- [52] D.-J. Zhang, H.-G. Li, Q.-L. Zhao, S. Wang, H.-B. Wang, J. Xiong, and K. Wang, Wavelength-multiplexing ghost imaging, *Phys. Rev. A* **92**, 013823 (2015).